Coastal Engineering 177 (2022) 104176

Contents lists available at ScienceDirect

Coastal Engineering

journal homepage: www.elsevier.com/locate/coastaleng

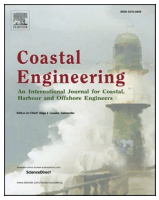

Transport properties of fast ice within the nearshore

S.E. Dodge [a,*], L.K. Zoet [a,b], J.E. Rawling III [c], E.J. Theuerkauf [d], D.D. Hansen [a]

[a] Department of Geoscience, University of Wisconsin-Madison, Madison, WI, USA
[b] Department of Civil and Environmental Engineering, Geological Engineering Program, University of Wisconsin-Madison, Madison, WI, USA
[c] Wisconsin Geological and Natural History Survey, University of Wisconsin-Madison, Madison, WI, USA
[d] Department of Geography, Environment, and Spatial Sciences, Michigan State University, East Lansing, MI, USA

ARTICLE INFO

Keywords:
Coastal geomorphology
Fast ice
Sediment entrainment
Sediment transport

ABSTRACT

Fast ice affects many coastlines in high- and mid-latitude regions, shaping the coastal morphology by acting as both a protective barrier from winter storms and as an erosive agent through sediment entrainment and transport. It has been hypothesized that when sediment-rich ice is dislodged and transported beyond the depth of closure by storm waves, sediment is permanently removed from the nearshore, starving the littoral system and facilitating future erosion. However, despite this large potential impact on coastal sediment budgets, the rates and mechanisms of sediment-rich ice transport are poorly constrained. This study investigates the sediment entrainment process by fast ice, the mechanisms needed for ice mobilization, and the force needed to breakup and transport sediment-rich ice. We find that the Coulomb frictional strength of the sediment regulates the fast ice system and that the viscous rheology of the ice has no direct mechanical effect. Importantly, these results show that only the frictional coefficient of the beach sediment needs to be measured to estimate the resistive strength of the fast ice, significantly simplifying the requirements for evaluating the potential for fast ice mobilization and associated sediment transport.

1. Introduction

Cold climate coasts represent more than 30% of the world's coastlines (Lantuit et al., 2011), but shore protection strategies often do not incorporate the effects of grounded icefoot complexes, referred to as fast ice, because the processes that regulate their contributions to coastal change are not well understood. Prior research has suggested winter fast ice both limits sediment transport, acting as a protective barrier from wave action in the nearshore (Marsh et al., 1973; Evenson and Cohn, 1979; BaMasoud and Byrne, 2012; Barnhart et al., 2014) and enhances sediment transport, acting as a primary driver for nearshore erosion (Miner and Powell, 1991; Barnes et al., 1994). While studies have investigated the amount of sediment within the series of ice ridges and lagoons found near the shore, commonly referred to as the nearshore ice complex (NIC) (McCormick et al., 1991; Barnes et al., 1993), none have quantitatively described the fundamental mechanics controlling nearshore fast ice entrainment and transport. The potential for ice to transport large volumes of sediment beyond the depth of closure, effectively removing sediment from the nearshore system (Evenson and Cohn, 1979; Miner and Powell, 1991), should be accounted for in coastal sediment budgets. This offshore transport occurs when sediment-rich ice blocks are mobilized during ice breakup, advected offshore as free-floating pack ice, and eventually melt (Reimnitz et al., 1991; Barnes et al., 1993, 1994). For example, in the Laurentian Great Lakes, most of the sediment deposited beyond the depth of closure is hypothesized to have been mobilized via ice processes (Reimnitz and Are, 2000). Estimates of sediment delivery to the deep lake basin by ice are roughly equal to the long-term supply of terrigenous sediment to the nearshore, suggesting that even subtle changes in sediment transport via ice could significantly affect the morphodynamics of cold-coast regions (Barnes et al., 1994).

Climate-change driven atmospheric warming and associated warming of oceans and large-lakes has resulted in, and will continue to induce, declines in the presence of winter shore ice as well as enhanced variability in ice dynamics, such as the timing of ice on/off (Filazzola et al., 2020; Bartosiewicz et al., 2021). As annual surface temperatures in the US and annual surface and ocean temperatures globally have risen in the last 50 years (EPA, 2021; NOAA, 2022), overall lake ice cover percentages have trended downwards in the Great Lakes (GLERL, 2021). These changes will alter patterns of coastal evolution and necessitate changes to shore protection strategies and coastal engineering designs; however, future predictions are limited by the current mechanistic understanding

* Corresponding author.
E-mail address: stefanie.dodge@wisc.edu (S.E. Dodge).

https://doi.org/10.1016/j.coastaleng.2022.104176
Received 3 February 2022; Received in revised form 12 May 2022; Accepted 9 July 2022
Available online 13 July 2022

of ice-associated sediment transport processes.

Previous studies of NICs have investigated their sediment composition, sediment entrainment in ice, and the impact of ice on coastal morphology. Significant volumes of entrained sediment have been observed in the NIC along freshwater coasts (Seibel et al., 1976; Barnes et al., 1993; Miner and Powell, 1991; Kempema and Holman, 1994). Nearshore erosion is enhanced when sediment-rich ice blocks from the icefoot of the NIC are dislodged during both winter storm events and ice breakup. These sediment-rich ice blocks are moved offshore as free-floating pack ice, resulting in sediment loss through lakeward transport to deeper waters (Reimnitz et al., 1991; Barnes et al., 1993, 1994). In marine settings, similar entrainment and transport processes have been observed along Arctic coastlines associated with sea ice and water-terminating glacial ice through the formation of an immobile icefoot (Short and Wiseman, 1974; Walker, 2005). Though ice formation along these coastlines does reduce the erosional impact of seasonal storm waves, the permanent removal of sediment from the nearshore by ice entrainment and rafting ultimately contributes to beach and bluff erosion along fresh and marine coastlines (Forbes and Taylor, 1994; Kelletat et al., 2013). However, there is limited data on these ice-associated sediment transport processes and no quantitative information on the mechanics of sediment entrainment and mobilization of debris-rich fast ice.

Previous studies have also examined the engineering properties of ice-block pileup in the context of offshore ice-pad construction by testing the frictional behavior of debris-free ice over unconsolidated sediments (Kovacs and Sodhi, 1980; Sodhi et al., 1983; Shapiro and Metzner, 1987; Zyryanov et al., 2002; Barker and Timco, 2003; Barrette and Timco, 2008; Leppäranta, 2013). Though the mechanics controlling the mobilization of debris-free ice blocks differ from those controlling fast ice with entrained debris, they provide bounding parameters for expected mobilization resistance. Many of these studies estimated friction by dragging large blocks of ice over sediment under different normal loads and measuring the resistance to slip (Sodhi et al., 1983; Shapiro and Metzner, 1987; Barker and Timco, 2003; Barrette and Timco, 2008). Reported coefficients of friction in these experiments span a wide range from 0.39 to 2.4 (see Barrette and Timco, 2008, and references therein). Dragging debris-free ice over sand, Barrette and Timco (2008) found that the system effectively behaved like a Coulomb material with a frictional coefficient of 0.39, which was lower than that of the sediment alone. However, they observed that friction values increased to a level comparable with the sand when stresses imposed by ice pileup caused the underlying sediment to deform.

Does fast ice with a debris-rich basal layer behave mechanically similar to a debris-free layer, or do the mechanical aspects of the basal debris significantly alter the system's mechanics? Given that fast ice can entrain large volumes of basal debris, understanding the conditions that mobilize it is important for constraining the potential contribution to coastal erosion. In this study, we examine sediment entrainment and mobilization associated with nearshore fast ice freeze-on. We combine observations of entrained sediment from nearshore sediment cores with laboratory experiments to examine the rates of sediment entrainment within the grounded icefoot and the physical mechanisms that regulate the mobilization of the sediment-rich ice.

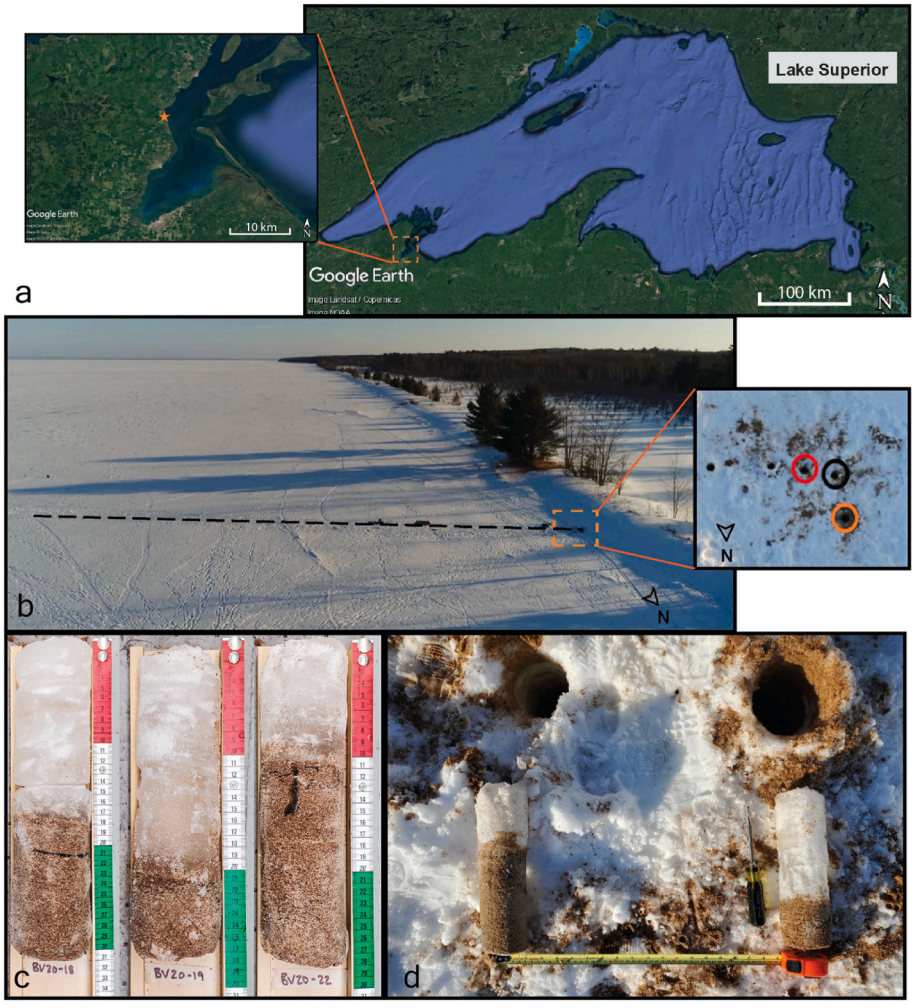

Fig. 1. a) Google Earth image of Lake Superior. The orange star on the zoomed-in image denotes our study site, Bayview Beach (46.747253, −90.883667). b) Aerial image of transect location (dashed black line) at Bayview Beach. The inset shows the location of the three ice cores collected within the shoreline. The black circle is core BV20-18; the red circle is core BV20-19; and the orange circle is core BV20-22. The ice core hole diameter measured 7.5 cm. Both of the images are looking S-SE. c) Three ice cores collected from the shoreline, BV20-18, BV20-19, and BV20-22 with visible sediment adhered to the base of each core. Ice cores BV20-18 and BV20-22 were sampled parallel to each other to collect a duplicate core. These cores were taken from water depths of 10–19 cm. d) A field image of ice cores BV20-22 (closer to shore) and BV20-19 showing decrease of frozen sediment lakeward. The cores in c) and d) were collected where the ice directly froze into the bed, meaning water depth was effectively 0 m in the winter months (no gap between the base of the ice and lakebed).

2. Study area and methods

To investigate sediment entrainment and mobilization processes associated with nearshore ice, we first collected ice cores along a roughly 75 m transect from Bayview Beach (BVB), a site located along the Lake Superior coast (Fig. 1a–*b*). BVB is a low-energy beach with persistent winter ice cover and no ice morphologic variability. We selected this site because of its history of consistent ice coverage and low energy wave conditions during winter (GLERL, 2021) and collected ice cores to quantify sediment content in the fast portion of the NIC. Rates of basal sediment entrainment were estimated with a 1-D Stefan Equation and compared to cores with sediment frozen to their base. Finally, sediment from the BVB site was sheared in a direct shear and a novel cryogenic ring shear apparatus to investigate mechanical controls on the strength of the nearshore fast ice portion of the NIC (e.g., ice, frozen sediment, and/or unfrozen sediment).

2.1. Ice cores

We obtained ice cores using a SIPRE hand auger drill with an attached Stihl BT-121 engine that collects samples up to 3 m in length in 1 m segments with a diameter of 7.5 cm. Three cores, collected near the shoreline at BVB, contained abundant beach sediment frozen to their base and spanned the boundary between frozen and thawed sediment (Fig. 1c). We observed a visible decrease in sediment freeze-on drilling lakeward (Fig. 1d). Ice thickness and water column depth were recorded through the core holes using a measuring rod. To determine the volume of the debris-rich portion of the BVB20-19 ice core, we isolated it and briefly submerged it in a graduated cylinder, while noting the change in water level. We then weighed the ice/sediment mixture, melted the ice, and subsequently weighed the leftover sand to determine porosity and bulk density for this portion of the core.

2.2. Stefan Equation

We used a 1-D solution of the Stefan Equation to estimate the depth of fast ice penetration into beach sediment (z_{max}) due to freeze-on from cold atmospheric conditions:

$$z_{max} = \lambda\sqrt{\frac{48knF}{L}} \tag{1}$$

where λ is a correction coefficient used in the modified Berggren formula to account for the effects of volumetric heat, k is the thermal conductivity of the frozen sand, n is an air-surface temperature correction factor, F is a freezing index factor that depends on atmospheric temperature, and L is volumetric latent heat of fusion of water (Table 1) (Aldrich, 1956; UFC, 2004; Roland et al., 2021). The values used for this calculation are based on a sediment porosity of 0.40 and a sediment/ice bulk density of 1.9 g/cm^3, which we measured directly from the BVB20-19 core. The Department of the Army and the Air Force defines freezing degree-days (FDD) as the difference between the average daily air temperature and 0 °C (TM Army, 1987). We estimated cumulative FDD at the BVB site for the interval spanning from 01/16/2020, the first day lake ice was observed, to 02/21/2020, when the cores were extracted. We set the freezing index (F) equal to the cumulative FDD, similar to the approach Kurylyk and Hayashi (2016) employed to predict maximum seasonal frost penetration depth. We then compared z_{max} to the observed thicknesses of the sediment-rich layers frozen to the base of the BVB cores (Aldrich, 1956; UFC, 2004; Kurylyk and Hayashi, 2016; Roland et al., 2021).

Table 1
A summary of the values used to calculate the depth of maximum ice penetration in the icefoot of the Nearshore Ice Complex.

Summary of values used to calculate the maximum ice penetration depth				
k [cal/m/°C/h]	n	λ	F [°C days]	L [cal/m^3]
1728	0.9	0.85	159	6.1 × 10^7

2.3. Direct shear

To constrain the internal angle of friction of the unfrozen beach sand (φ_{DS}), we conducted direct shear experiments in an ELE International device (Fig. 2a), following ASTM standard 3080 (ASTM D3080/D3080M-11, 2011). Sand from BVB (which is identical to the material entrained in the ice cores) was first dried and sieved using a #10 (2 mm) screen, which removed ~2% of the total sample by weight. The stainless-steel sample chamber (sized 10 × 10 × 2 cm) consisted of two halves of equal thickness divided horizontally. The sample box was filled with BVB sand and mounted in the direct shear device (Fig. 2b) under a loading platen. We then applied a prescribed normal stress, σ_N, to the sample using a leveraged weight. During shear, the upper portion of the sample was held stationary while an actuated ram drove the bottom half horizontally. This produced a shear force that mobilized sand particles to create a shear plane. The sample was sheared at a constant rate (2–3 mm/min) for a displacement of ~1 cm, while an inline load cell measured the shear force at 1-s intervals. Normal stress was calculated as:

$$\sigma_N = \frac{10 \cdot W \cdot g}{A} \tag{2}$$

where W is the leverage weight, g is the gravitational constant, A is the area of the shear box, and 10 is the leveraging ratio provided by the moment arm. Because the sample was dried prior to shear, there was no pore water pressure, so σ_N equals the effective normal stress, σ'_{DS}. Mean critical state shear strength of the sand (τ_{DS}) was calculated from the measured shear force as:

$$\tau_{DS} = \frac{LC \cdot g}{A} \tag{3}$$

where LC is the mean resistive force measured by the load cell over an interval when deformation reached critical state.

Following this protocol, six experiments were completed over a range of σ'_{DS} (20, 39, 78, 118, 177, and 255 kPa). From these results, we calculated φ_{DS} as the arctangent of the slope of a linear regression between σ'_{DS}–τ_{DS}. Grain size distribution of the BVB sample was measured with a Malvern Mastersizer 2000E and determined to be poorly graded, coarse-grained sand with a modal grain diameter of 0.788 mm.

2.4. Ring shear

We used a novel cryogenic ring shear device (Fig. 3a–*b*) to simulate the shearing of a frozen ice/sediment block over an unfrozen saturated sediment bed. This experiment tested if the slip resistance of sediment-rich ice is mechanically controlled by the ice, the sediment, or some combination of both. The ring shear device resides in the Surface Processes walk-in freezer at UW-Madison's Department of Geoscience (see Hansen and Zoet, 2022 for instrumentation detail). Cryogenic ring shear studies have provided valuable insights into ice-bed mechanics within glaciology (Zoet and Iverson, 2015, 2016, 2018, 2020; Zoet et al., 2021; Hansen and Zoet 2022), but they have not been employed in coastal studies prior to this work. The annular sample chamber (inner diameter = 0.2 m; outer diameter = 0.6 m; height = 0.3 m) sits in a temperature-controlled glycol/water bath, regulated by an external circulator at ~0.01 °C precision. The sample chamber has an aluminum baseplate lined with a rubber mat to minimize slip at the bottom boundary. Twelve drainage tubes evacuate water from the chamber as the sample contracts under pressure, ensuring drained conditions.

We placed a 12-cm-thick layer of BVB sand at the base of the sample chamber and then filled the sample chamber with deionized water until

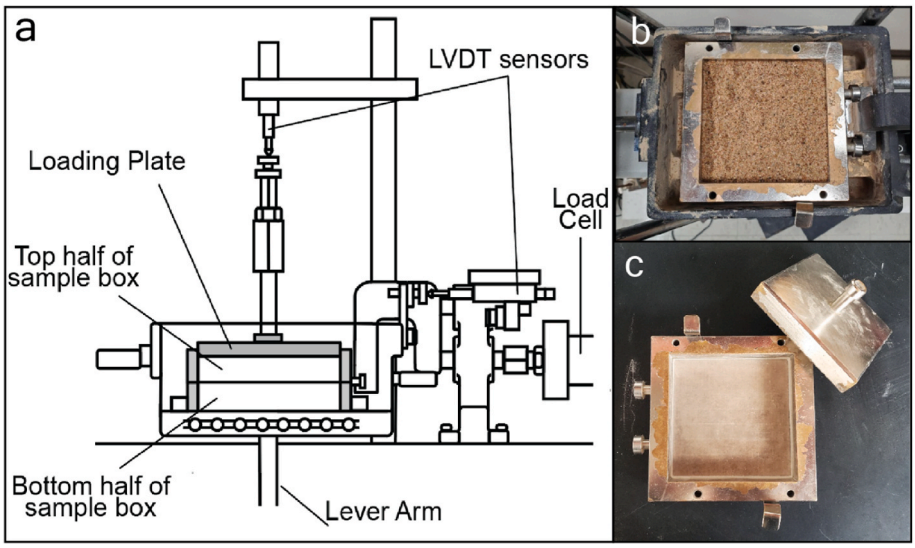

Fig. 2. a) Design schematic of the direct shear device. b) The 10 cm × 10 cm sample chamber was filled with dried, sieved BVB sand. c) Sample chamber with acrylic plate placed in the bottom half.

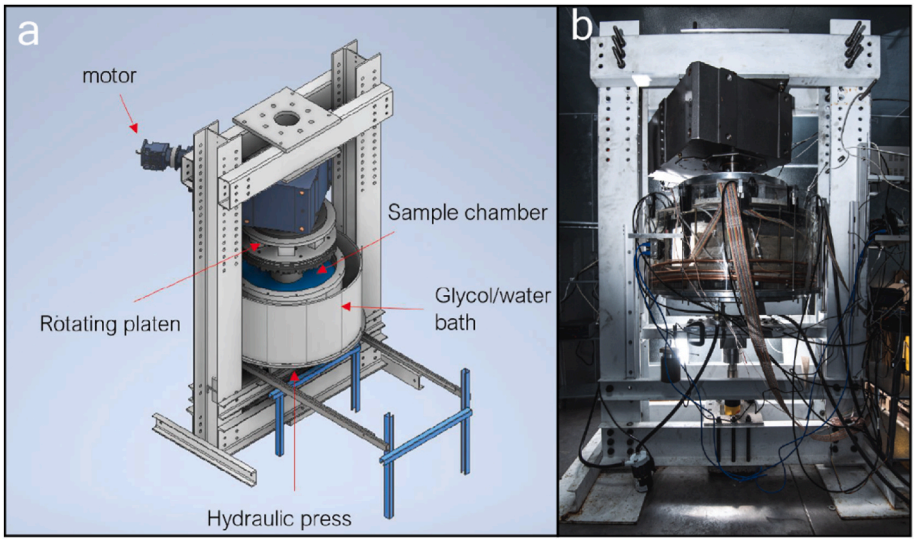

Fig. 3. a) Design schematic of the ring shear device. b) Operational ring shear with sample chamber lifted into the rotating platen (Image: Ethan Parrish).

the water level was ~10 cm above the surface of the sand. At the start of the experiment, we set the height of the glycol bath level with the sand and the bath temperature to 6.5 °C to simulate heat stored in the lakebed from warmer months. Similarly, the ambient temperature in the walk-in freezer was set to −10 °C to simulate cold winter atmospheric temperatures. This temperature gradient initiated a freezing front that migrated from the top down toward the sediment bed. As ice approached the sand, we lowered the glycol bath to a point 5 cm below the sand-ice interface (Fig. 4a), which allowed the water column to freeze entirely and ice to penetrate the top layer of sediment. In this configuration, the upper layer of the exposed sand froze to a depth of ~2.0 cm while a thawed sand layer persisted at the base of the sample chamber (Fig. 4b)—analogous to a fast-freezing front migrating into lake sediments during cold winter conditions (see Fig. 1). When the frozen/thawed boundary reached its steady state position, we raised the glycol bath level to the top of the sample chamber, set the bath temperature to 0.2 °C, and raised the ambient freezer temperature to 0 °C. This thermal condition induced a small amount of melt around the perimeter of the sample chamber, which minimized drag from the ice against the acrylic walls.

At this stage of the experiment, a normal stress was applied to the sample via a vertical ram, and slip was initiated by rotating the upper platen at a constant rate of 99.5 m/yr. This forced the frozen ice/sediment layer to shear atop the unfrozen sediment in the base of the sample chamber, mimicking the mobilization of a fast ice block in nature. Cameras mounted on the outer wall monitored the movement of sand through clear acrylic walls, confirming that slip occurred along this frozen/thawed sediment boundary. A torque sensor mounted along the central axis recorded resistance to shear, and three pressure transducers installed in the sidewalls measured the pore water pressure. Once torque reached its steady state following each stress step, we stopped the experiment and relieved the torque by spinning the rotating platen backwards until torque reached its original resting value. This process was repeated for six effective stresses, σ'_{RS} ~55, 99, 100, 116, 143, and 190 kPa, reported here as the mean normal stress applied to the ice ring over an interval during which critical state deformation occurred minus the concurrent average pore water pressure.

In the ring shear, mobilized sediment (both thawed and frozen) supplied boundary drag as it sheared against the acrylic walls. To isolate

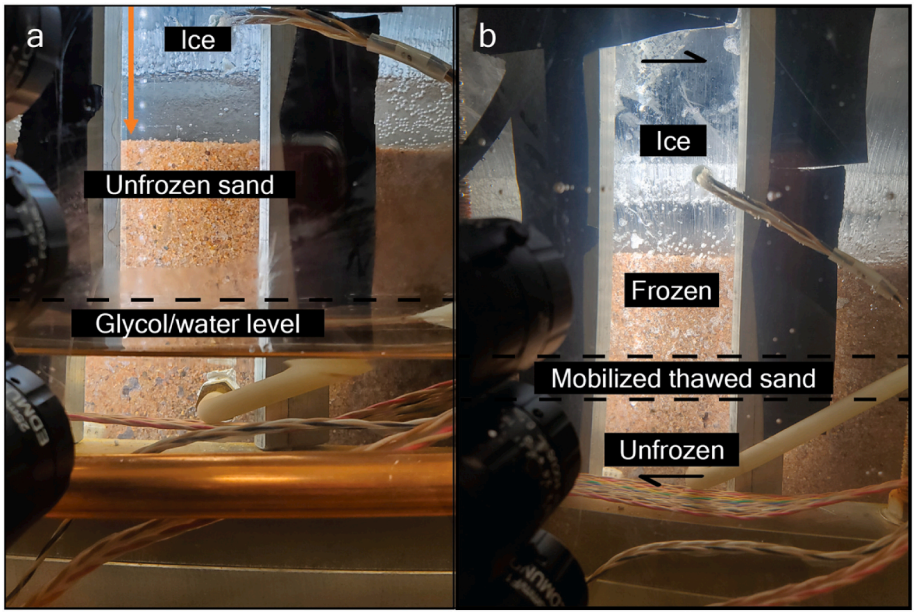

Fig. 4. *a) The glycol/water mixture is lowered* 5 cm *below the top of the sand. The water freezes from the top down, allowing the ice to penetrate into the unfrozen sand bed similar to fast ice. b) Ice grows from the top of the sample chamber down into the sediment bed. The frozen/unfrozen boundary was observed ~2.0* cm *below the top of the sand.*

drag induced at the slip interface between frozen/thawed sediment, we subtracted this wall drag (calculated separately for the thawed and frozen sections) from the overall torque record. For the thawed deforming layer (~1.4 cm thick) subjacent to the frozen sand/ice block, we followed a protocol similar to Zoet and Iverson (2018). First, we measured the frictional coefficient of BVB sand against an acrylic plate in the direct shear (~0.29, Fig. 2c) over a range of normal stresses (σ_N = 19–157 kPa). We then calculated the torque imposed by drag at the inner/outer boundaries by multiplying the measured frictional coefficient for sand on acrylic by: i) the horizontal effective stress, ii) the respective contact area (inner or outer circumference × thickness of the mobilized layer), and iii) the respective inner or outer radius. We estimated the horizontal effective stress by multiplying σ'_{RS} by a factor, $s = (1\text{-}sin(\varphi_{DS}))\ \sqrt{OCR}$, where OCR is the over consolidation ratio (here equal to 1), and φ_{DS} is the friction angle of the BVB sediment measured in the direct shear. For the layer of frozen sand (~2 cm thick), we employed a similar approach with one key difference—we assumed horizontal stress was similar to that of a confined elastic solid cylinder under uniaxial compression, where horizontal stress equals $(\sigma'_{RS}\,\nu)/(1\text{-}\nu)$ and $\nu = 0.4$ represents Poisson's ratio of a saturated ice/sand mixture near the pressure melting point (Christ and Park, 2009; Christ et al., 2009; Park and Lee, 2014). We subtracted torque induced by the combined wall drag at the inner/outer boundaries from the overall torque measurements, resulting in a corrected torque, *T,* that relates solely to frozen/thawed sediment interactions. We then converted T to a shear stress, τ_{RS}, using an analytical solution for torque integrated over an annular disc with respect to radial position:

$$\tau_{RS} = \frac{3}{2\pi}\cdot\frac{T}{(R_o)^3(R_i)^3} \tag{4}$$

where R_i = 0.1 m and R_o = 0.3 m are the inner and outer radii of the sample chamber respectively.

Similar to the direct shear experiments, we computed the internal angle of friction for the ring shear experiments, φ_{RS} , from the arctangent of the slope of a linear regression between σ'_{RS} and τ_{RS}. By comparing φ_{RS} with φ_{DS} , we can ascertain if the two contrasting systems (i.e., dry sand versus frozen/thawed saturated sediment) exhibit similar frictional properties and thereby identify the mechanisms controlling the resistive strength of a debris-rich ice block resting on a thawed sediment bed. We note that because of the presence of ice, it was unknown at the onset of the experiment if the σ'_{RS}–τ_{RS} relationship would be linear (Coulomb) or non-linear (have a viscous component).

3. Results

3.1. Sediment properties and Stefan Equation

Sediment and ice mass in the debris-rich portion of the sediment core BVB20-19 (Fig. 1c) were 411 g and 99 g respectively. The volume of the sediment-rich section of this core was 260 cm^3, and the density of the BVB sand was 2.61 g/cm^3. Using these values, we estimate that the porosity and the bulk density of the sediment-rich ice layer in the core was 0.40 and 1.9 g cm^{-3}, respectively. For comparison, we also measured the porosity of BVB sediment with no ice or water in the pore space after it was consolidated under a load approximately equal to the weight of ice overburden inferred from our cores (σ_N ~ 0.5 kPa). This dry porosity was 0.39, nearly identical to the porosity of the debris-rich ice.

Implementing the parameter values in Table 1, Equation (1) predicts a maximum ice penetration depth of 0.37 m between the time of shore ice formation in January 2020 and core retrieval in February 2020. Our use of Equation (1), however, does not account for the conduction of heat through the pure ice layer atop the freezing sediment or the addition of stored heat from lower sediment layers. Therefore, our Stefan solution should be viewed as a maximum depth and only used as a first-order approximation. Indeed, cores collected closest to the shore show ice only penetrated the sediment to depths of 0.18 m and 0.13 m. Adhered sediment thickness has a nonlinear trend with time (Eq. (1)). The observed discrepancy between predicted z_{max} and the observed depths of ice penetration is in part due to the difficulty of extracting heat from the pore volume water at depth, as distance from the cold atmosphere increases.

3.2. Direct shear and ring shear

In both the direct shear and ring shear experiments, τ increased linearly with increasing σ' (Fig. 5), indicating Coulomb behavior (i.e., $\tau = \sigma' tan\varphi$). Steady-state friction angles are effectively the same for both devices within estimated uncertainty: φ_{DS} ~30.5 ± 1.7° compared to

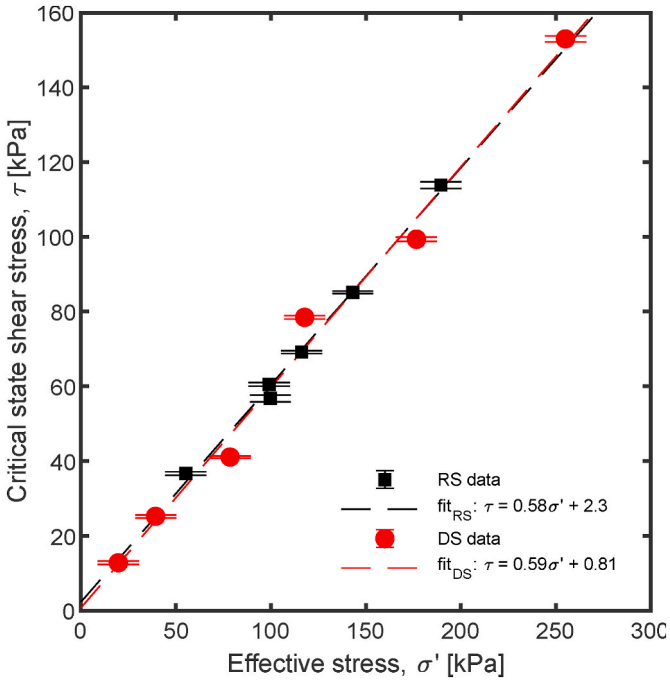

Fig. 5. Critical state shear stress varies linearly with effective stress for both the ring shear (black squares) and direct shear (red circles) experiments, indicating Coulomb frictional behavior. Dashed lines show linear regressions computed for the respective data ($R^2 \sim 0.99$ for both fits). All reported values for shear stress and the ring shear effective stresses are averages calculated over an interval when deformation was at critical state. Effective stresses for the direct shear are applied by weights hung from a lever arm and not measured directly. Vertical error bars denote the standard deviation. Horizonal error bars for effective stress are smaller than the marker width and omitted for clarity.

φ_{RS} $\sim 30.2 \pm 1.2°$. (Stated uncertainties here represent the arctangent of the standard error associated with the slope of linear regression between $\sigma' - \tau$ with associated p-values for the coefficient $<10^{-4}$). Both linear fits give y-intercepts slightly greater than zero (2.3 ± 2.7 kPa and 0.81 ± 4.2 kPa for ring shear and direct shear data, respectively). However, in both cases, the magnitude of the y-intercept is smaller than the associated standard error (reported here as plus-or-minus values), and the corresponding p-values $\gg 0.05$, indicating the intercept coefficients are not statistically significant. Furthermore, since BVB sand is poorly-graded and coarse-grained, we assume that cohesive strength is negligible and the true intercept in σ'–τ space is likely zero (Lambe and Whitman, 1969).

In the ring shear experiment, we visually observed that the slip interface between frozen and thawed sediment occurred at a depth ~2.0 cm below the surface of the sand bed. Sediment frozen to the base of the ice ring moved as a coherent block superjacent to a thin layer of deforming sand ~1.4 cm thick. Beneath this deforming layer, the sand bed was stationary.

4. Discussion

The close match in friction angles between the direct shear and ring shear experiments (Fig. 5) demonstrates that sediment at the base of the frozen layer of fast ice regulates the mobilization strength of the system and that ice has no direct mechanical effect on the resistive stresses. It was previously unknown if the fast ice would break within the ice itself, at the boundary between debris-free and debris-rich ice, or at the frozen/thawed boundary. In our ring shear experiments, the "weak link" was clearly the frozen/thawed boundary (Fig. 4b), and resistance to slip exhibited a Coulomb response. It therefore follows that blocks of ice with sediment adhered to their base slipping over a thawed bed can be treated as a Coulomb material with a friction angle equal to that of the sediment. This observation has implications for nearshore sediment transport since sediment-laden ice blocks can travel beyond the depth of closure when mobilized. Importantly, because the friction angle of the beach sediment controls resistance to motion, similar analysis can be done elsewhere simply by measuring this parameter—a much less onerous process than conducting cryogenic ring-shear experiments.

The coefficient of friction we measured for debris-rich ice slipping atop thawed sediment (0.58–0.59) is higher than the value Barrette and Timco (2008) reported for debris-free ice (0.39). This indicates that in locations where debris-free ice abuts debris-rich basal ice, the sediment-rich ice provides more resistive stress. Furthermore, the wide range of frictional coefficients previously observed in ice-on-sediment slip experiments can be reinterpreted from our observations. Since the transparent sample chamber walls of the ring shear reveal the precise location of the slip interface, we can clarify previous ambiguities. Experiments with reported friction coefficients less than the strength of the underlying sediment truly measured debris-free ice slipping atop the bed; whereas those with friction coefficients nearly equal to the sediment likely had basal debris adhered to the base of the ice block. Experiments with very high friction coefficients were likely partially frozen to the base of the sample chamber. Sediment entrainment within the ice block increases the resistive stress in a manner akin to the ice-rubble "skirting" effect proposed by Weaver et al. (1991) to protect offshore structures.

Knowing the mechanical properties regulating the system, we can estimate wave heights needed to mobilize subaerial ice/sediment blocks. The resistive stress provided by the weight of the ice/sediment block and φ can be estimated from laboratory experiments to resolve the minimum wave height, H, required for dislodgement and mobilization. We follow Nott's (2003) treatment of forces needed to mobilize a subaerial boulder but, importantly, modify his resistive stress equation to one of Coulomb frictional resistance, f_s, in accordance with our findings: $f_s = abc\rho_{bb}g\mu$, where ρ_{bb} is the average bulk density of the ice/sediment block, $\mu = tan\varphi$ is the measured coefficient of friction, a is the width of the block, b is the length of the block, c is the height of the block, and g is the gravitational constant. We solve Nott's equations (1)–(3) and our new f_s (in place of their equation (4)) to produce a new version of their equation 25 for a Coulomb material. We note that Nott made an algebraic error in their paper which we have fixed here.

$$H \geq \frac{\rho_{bb}abcg\mu - 2C_m\rho_w abc\ddot{u}}{0.25\,\rho_w(C_d ac^2 + C_l cb^2)\delta g} \tag{5}$$

We set $\mu = 0.59$, which equals the tangent of our measured internal angle of friction from the direct shear ($\varphi_{DS} = 30.5°$). We implement height parameters ($c = 0.27$ m) for the ice block based on the values measured in the BVB20-19 core (Fig. 1c) for a unit area (a, $b = 1$ m). We use the measured bulk density from the sediment-rich portion of the core (1.9 g/cm^3) and the density of ice (0.92 g/cm^3) to estimate a bulk density for the block, $\rho_{bb} = 1.17$ g/cm^3 based on the core dimensions (20 cm of ice, 7 cm of debris laden ice). We take the parameters for the coefficients of mass (C_m), drag (C_d), lift (C_l), instantaneous flow acceleration ($\ddot{u}$), and wave transformation (δ) from Nott (2003). Using these parameters, we estimate the critical wave height needed to dislodge the ice block in terms of frictional resistance instead of rotational moment. We estimate that under favorable thermal conditions the critical wave height needed is $H \sim 1.6$ m. Despite the many assumptions of this model, it serves as a preliminary attempt to link wave characteristics to the potential for sediment-laden ice transport. These results indicate that with Coulomb friction of the underlying sediment regulating the detachment strength of ice/sediment blocks, the mobilization of fast ice could occur with moderate wave conditions for our study site. Wave heights of this magnitude occur regularly in the Great Lakes (e.g., Davidson-Arnott and Pollard, 1980; Booth, 1994) and are even more likely in marine settings due to the larger fetch.

Based on the results of this study, if waves of sufficient magnitude are

present during an ice breakup event, mobilization of sediment-rich ice in the nearshore is likely. If offshore winds occur during or shortly after the breakup, sediments encased in ice can potentially be rafted to deeper waters, deposited beyond the depth of closure, and removed from the nearshore sediment budget. Colder, more persistent winter conditions will drive ice penetration deeper into the lakebed, allowing for a higher volume of sediment to become entrained within the ice. However, these conditions also favor a more extensive NIC that may only breakup once per season, which could lower the probability of ice block dislodgement and transport offshore by multiple winter storm events. Warmer, shorter winters will decrease ice penetration and reduce the amount of sediment that can be entrained in the icefoot, but these conditions may result in multiple icefoot build-up and break-up events due to a less extensive NIC, increasing the potential for offshore movement of sediment-laden ice. Interestingly, due to the nonlinear nature of the Stefan solution and the greater number of NIC breakup and reformation events in milder, cold-coast settings, maximum sediment loss may not occur in the coldest freezing climates but rather in those that lie in an intermediate range.

5. Conclusion

Winter fast ice in cold climate environments can significantly impact coastal geomorphic evolution if debris-rich ice is dislodged and rafted out to deeper waters, permanently removing sediment from the littoral system. Here we show that a substantial amount of sediment can be frozen into ice in areas where ice is in direct contact with the bed. We also show that the system is mechanically regulated by the frozen/thawed sediment contact and effectively behaves as a Coulomb material despite the viscous rheology of the ice. This means that only the friction angle of the beach sediment needs to be measured to estimate the resistive strength of the fast ice, significantly reducing the complexity of evaluating potential sediment entrainment and transport in cold coast regions. Wave heights required to move such sediment-rich ice blocks are modest, and if wave height/energy is large enough, ice blocks with entrained sediment can be transported offshore to deposit sediment beyond the depth of closure.

Open research section

The data files collected for the ring shear and direct shear experiments along with the porosity and wave height codes used in the study are available at the MINDS@UW repository https://minds.wisconsin.edu/handle/1793/83359.

CRediT author statement

Stefanie Dodge: Methodology, Visualization, Formal Analysis, Investigation, Data curation, Resources, Writing (original draft), Writing (review & editing).

Lucas Zoet: Conceptualization, Methodology, Visualization, Investigation, Validation, Resources, Writing (original draft), Writing (review & editing), Supervision, Project administration, Funding acquisition.

J. Elmo Rawling III: Conceptualization, Investigation, Writing (original draft), Writing (review & editing), Supervision, Project administration, Funding acquisition.

Ethan Theuerkauf: Conceptualization, Writing (original draft), Project administration, Funding acquisition.

Dougal Hansen: Methodology, Software, Formal Analysis, Data curation, Validation, Resources, Writing (original draft), Writing (review & editing).

Declaration of competing interest

The authors declare that they have no known competing financial interests or personal relationships that could have appeared to influence the work reported in this paper.

Acknowledgments

This project was funded by the National Science Foundation Award Number EAR-1916179 awarded to L.K. Zoet, J.E. Rawling, and E.J. Theuerkauf. Special thanks to Peter Sobol and Neal Lord for their work designing the ring shear device. Additional thanks to Luke Milner and Will Tuttle for field assistance, and the U.S. Ice Drilling Program for use of the ice core drill.

References

Aldrich Jr., H.P., 1956. Frost penetration below highway and airfield pavements. Highw. Res. Board Bull. 135. https://trid.trb.org/view/128066.

TM Army, 1987. Technical Manual Arctic and Subarctic Construction General, Technical Manual, vol. 1. Departments of the Army and the Air Force, Washington, DC. TM 5-852-1/AFR 88-19.

ASTM D3080/D3080M-11, 2011. Standard Test Method for Direct Shear Test Od Soils under Consolidated Drained Conditions (Withdrawn 2020). ASTM International, West Conshohocken, PA. DOI: 10.1520.D3080_D3080M-11. www.astm.org.

BaMasoud, A., Byrne, M.-L., 2012. The impact of low ice cover on shoreline recession: a case study from Western Point Pelee. Canada. Geomorphology 173–174, 141–148. https://doi.org/10.1016/j.geomorph.2012.06.004.

Barker, A., Timco, G., 2003. The Friction Coefficient of a Large Ice Block on a Sand/Gravel Beach.

Barnes, P.W., Kempema, E.W., Reimnitz, E., McCormick, M., Weber, W.S., Hayden, E.C., 1993. Beach profile modification and sediment transport by ice: an overlooked process on lake Michigan. J. Coast Res. 9, 65–86. https://www.jstor.org/stable/4298069.

Barnes, P.W., Kempema, E.W., Reimnitz, E., Mccormick, M., 1994. The influence of ice on southern lake Michigan coastal erosion. J. Great Lake. Res. 20, 179–195. https://doi.org/10.1016/s0380-1330(94)71139-4.

Barnhart, K.R., Overeem, I., Anderson, R.S., 2014. The effect of changing sea ice on the physical vulnerability of Arctic coasts. Cryosphere 8, 1777–1799. https://doi.org/10.5194/tc-8-1777-2014.

Barrette, P.D., Timco, G.W., 2008. Laboratory study on the sliding resistance of level ice and rubble on sand. Cold Reg. Sci. Technol. 54 (2), 73–82. https://doi.org/10.1016/j.coldregions.2008.02.002.

Bartosiewicz, M., Ptak, M., Woolway, R.I., Sojka, M., 2021. On thinning ice: effects of atmospheric warming, changes in wind speed and rainfall on ice conditions in temperate lakes (Northern Poland). J. Hydrol. 597, 125724.

Booth, J.S., 1994. Wave climate and nearshore lakebed response, Illinois beach state Park, lake Michigan. J. Great Lake. Res. 20, 163–178. https://doi.org/10.1016/s0380-1330(94)71138-2.

Christ, M., Park, J.B., 2009. Ultrasonic technique as tool for determining physical and mechanical properties of frozen soils. Cold Reg. Sci. Technol. 3 (58), 136–142. https://doi.org/10.1016/j.coldregions.2009.05.008.

Christ, M., Kim, Y.C., Park, J.B., 2009. The influence of temperature and cycles on acoustic and mechanical properties of frozen soils. KSCE J. Civ. Eng. 13 (3), 153–159. https://doi.org/10.1007/s12205-009-0153-1.

Davidson-Arnott, R.G.D., Pollard, W.H., 1980. Wave climate and potential longshore sediment transport patterns, Nottawasaga Bay, Ontario. J. Great Lake. Res. 6, 54–67. https://doi.org/10.1016/s0380-1330(80)72082-8.

EPA (Environmental Protection Agency), 2021. Climate Change Indicators: U.S. And Global Temperature. Retrieved from. https://www.epa.gov/climate-indicators/climate-change-indicators-us-and-global-temperature.

Evenson, E.B., Cohn, B.P., 1979. The Ice-foot Complex: its morphology, formation, and role in sediment transport and shoreline protection. Ann. Geomorphol. 23 (58–75). ISSN#: 0372-8854.

Filazzola, A., Blagrave, K., Imrit, M.A., Sharma, S., 2020. Climate change drives increases in extreme events for lake ice in the Northern Hemisphere. Geophys. Res. Lett. 47 (18), e2020GL089608.

Forbes, D.L., Taylor, R.B., 1994. Ice in the shore zone and the geomorphology of cold coasts: progress in Physical Geography. Earth Environ. 18, 59–89. https://doi.org/10.1177/030913339401800104.

GLERL, 2021. Ice Cover. Ice Cover. NOAA Great Lakes Environmental Research Laboratory -, Ann Arbor, MI, USA. Retrieved from. https://www.glerl.noaa.gov/data/ice/.

Hansen, D.D., Zoet, L.K., 2022. Characterizing sediment flux of deforming glacier beds. J. Geophys. Res.: Earth Surf. 127 (4) https://doi.org/10.1029/2021jf006544.

Kelletat, D.H., Scheffers, A.M., May, S.M., 2013. Coastal Environments from Polar Regions to the Tropics: a Geographer's Zonality Perspective, vol. 388. Geological Society, London, Special Publications, pp. 33–57. https://doi.org/10.1144/sp388.1.

Kempema, E.W., Holman, R.A., 1994. Video monitoring of nearshore ice in southern lake Michigan. J. Great Lake. Res. 20, 196–205. https://doi.org/10.1016/s0380-1330(94)71140-0.

Kovacs, A., Sodhi, D.S., 1980. Shore ice pile-up and ride-up: field observations, models, theoretical analyses. Cold Reg. Sci. Technol. 2, 210–288. https://doi.org/10.1016/0165-232x(80)90076-2.

Kurylyk, B.L., Hayashi, M., 2016. Improved stefan equation correction factors to accommodate sensible heat storage during soil freezing or thawing. Permafr. Periglac. Process. 27, 189–203. https://doi.org/10.1002/ppp.1865.
Lambe, T.W., Whitman, R.V., 1969. Soil Mechanics: Series in Soil Engineering. John Wiley & Sons, pp. 137–150.
Lantuit, H., Overduin, P.P., Couture, N., Wetterich, S., Aré, F., Atkinson, D., Brown, J., Cherkashov, G., Drozdov, D., Forbes, D.L., Graves-Gaylord, A., Grigoriev, M., Hubberten, H.-W., Jordan, J., et al., 2011. The arctic coastal dynamics database: a new classification scheme and statistics on arctic permafrost coastlines. Estuar. Coast 35, 383–400. https://doi.org/10.1007/s12237-010-9362-6.
Leppäranta, M., 2013. Land–ice interaction in the Baltic sea. Est. J. Earth Sci. 62 (1), 2–14. https://doi.org/10.3176/earth.2013.01.
Marsh, W.M., Marsh, B.D., Dozier, J., 1973. Formation, structure, and geomorphic influence of Lake Superior icefoots. Am. J. Sci. 273, 48–64. https://doi.org/10.2475/ajs.273.1.48.
McCormick, M., Kempema, E.W., Haines, J.W., Barnes, P.W., Reimnitz, E., 1991. Southern Lake Michigan Coastal Ice and Sediment Sample Data: Shoreface and Ice Profiles (Winter 1990/91). U.S. Department of the Interior. https://doi.org/10.3133/ofr91619b. U.S. Geological Survey. Open-File Report 91-619-A.
Miner, J.J., Powell, R.D., 1991. An evaluation of ice-rafted erosion caused by an icefoot complex, southwestern lake Michigan. U.S.A. Arctic Alpine Res. 23, 320–327. https://doi.org/10.2307/1551610.
NOAA (National Oceanic and Atmospheric Administration), 2022. Climate at a Glance. National Climatic Data Center. Retrieved April 2022, from. https://www.ncdc.noaa.gov/cag/global/time-series/globe/land_ocean/ann/12/1880-2022.
Nott, J., 2003. Waves, coastal boulder deposits and the importance of the pre-transport setting. Earth Planet Sci. Lett. 210, 269–276. https://doi.org/10.1016/s0012-821x(03)00104-3.
Park, J.H., Lee, J.S., 2014. Characteristics of elastic waves in sand–silt mixtures due to freezing. Cold Reg. Sci. Technol. 99, 1–11. https://doi.org/10.1016/j.coldregions.2013.11.002.
Reimnitz, E., Are, F.E., 2000. Coastal bluff and shoreface comparison over 34 Years indicates large supply of erosion products to arctic seas. Polarforschung 68, 231–235.
Reimnitz, E., Hayden, E., McCormick, M., Barnes, P.W., 1991. Preliminary observations on coastal sediment loss through ice rafting in lake Michigan. J. Coast Res. 7, 653–664. https://www.jstor.org/stable/4297883.
Roland, C.J., Zoet, L.K., Rawling, J.E., Cardiff, M., 2021. Seasonality in cold coast bluff erosion processes. Geomorphology 374. https://doi.org/10.1016/j.geomorph.2020.107520.
Seibel, E., Carlson, C.T., Maresca, J.W., 1976. ice ridge formation: probable control by nearshore bars. J. Great Lake. Res. 2, 384–392. https://doi.org/10.1016/s0380-1330(76)72301-3.
Shapiro, L.H., Metzner, R.C., 1987. Coefficients of friction of sea ice on beach gravel. J. Offshore Mech. Arctic Eng. 109 (4), 388–390. https://doi.org/10.1115/1.3257036.
Short, A.D., Wiseman, W.M.J., 1974. Freeze-up processes on arctic beaches. Arctic 27. https://doi.org/10.14430/arctic2875.
Sodhi, D.S., Hirayama, K., Haynes, F.D., Kato, K., 1983. Experiments on ice ride-up and pile-up. Ann. Glaciol. 4, 266–270. https://doi.org/10.3189/s0260305500005589.
UFC, 2004. Calculation Methods for Determination of Depths of Freeze and Thaw in Soils- Arctic and Subarctic Construction. Departments of the Army and the Air Force, Washington, DC. Technical Manual TM 5-852-6/AFR 88-19, vol. 6.
Walker, H.J., 2005. Ice-bordered coasts. In: The Encyclopedia of Coastal Science. Springer, Dordrecht, Switzerland, pp. 1003–1010.
Weaver, J.S., Poplin, J.P., Croasdale, K.R., 1991. Spray ice islands for exploration in the Canadian Beaufort Sea. In: Proceedings of the 10th International Conference on Offshore Mechanics and Arctic Engineering (OMAE), 4. The American society of mechanical Engineers (ASME), Stavanger, Norway, pp. 17–22.
Zoet, L.K., Iverson, N.R., 2015. Experimental determination of a double-valued drag relationship for glacier sliding. J. Glaciol. 61 (225), 1–7. https://doi.org/10.3189/2015JoG14J174.
Zoet, L.K., Iverson, N.R., 2016. Rate-weakening drag during glacier sliding. J. Geophys. Res.: Earth Surf. 121 (7), 1206–1217. https://doi.org/10.1002/2016JF003909.
Zoet, L.K., Iverson, N.R., 2018. A healing mechanism for stick-slip of glaciers. Geology 46 (9), 807–810.
Zoet, L., Iverson, N., 2020. A slip law for glaciers on deformable beds. Science 368 (6486), 76–78. https://doi.org/10.1126/science.aaz1183.
Zoet, L.K., Iverson, N.R., Andrews, L., Helanow, C., 2021. Transient evolution of basal drag during Glacier Slip. J. Glaciol. 1 https://doi.org/10.1017/jog.2021.131. –10.
Zyryanov, D., Divine, D., Korsnes, R., 2002. Mechanical Simulation of Shore Fast Ice Break-Up: Kara and Laptev Seas.